Loop antenna over a conducting cone with a spherical cap

Prasanta Halder[1], Bratin Ghosh[1] ✉, S.K. Moinul Haque[1], Kamal Sarabandi[2]

[1]*Department of Electronics and Electrical Communication Engineering, Indian Institute of Technology, Kharagpur, West Bengal 721 302, India*
[2]*Department of Electrical and Computer Engineering, University of Michigan, Ann Arbor, MI 48109 2122, USA*
✉ *E-mail: bghosh@ece.iitkgp.ac.in*

Abstract: A composite antenna structure consisting of a conducting cone loaded with a spherical cap is designed and analysed, considering all eigenmodes in the antenna structure. The configuration is used to enhance the impedance match to a loop antenna located above the cone tip. Matching characteristics to the loop are examined over a wide range of loop radius and loop location. It is found that the matching to the loop can be significantly enhanced over a wide range of parameter values, yielding a greater flexibility in design than the loop-around-the-cone structure presented earlier with the conducting cone body inside the loop. The structure also enables placement of the loop at a greater height than the loop-around-the-cone configuration, potentially improving the efficiency of signal transmission/reception or reducing scattering from the vehicular body. The mutual coupling effect of a parasitic loop placed adjacent to the primary loop is also analysed. The radiation characteristics are also evaluated.

1 Introduction

Circular loop antennas have been an area of active research in the past. However, in the analysis of such antenna structures, the loop current has been assumed constant in many investigations without considering higher-order modes that can significantly affect the antenna characteristics, particularly for antennas whose dimensions are comparable with a wavelength. A number of previous works taking into account a non-uniform loop current deal with the performance of the loop antenna in free space [1–7].

Circular loop antennas in the vicinity of discontinuities have been reported for circular loops near a planar interface [8, 9], a resistive sheet [10] or above a lossless ground plane [11]. Loop antennas near the conducting and dielectric spherical structures were investigated in [12, 13]. Although the radiation characteristics of the loop antenna were examined in [12, 13], the reflection coefficient and coupling characteristics of the antenna structures were not investigated. A conformal slot [14] and a microstrip patch antenna [15] located on a conical structure were analysed using the reciprocity theorem. A biconical microstrip antenna was investigated in [16].

Analysis of an antenna configuration consisting of multiple loops around a conducting cone was reported in [17], which could be used in a number of practical applications. Particularly, the matching characteristics of the loop antenna relative to an isolated loop were significantly improved by the presence of the cone. An improvement in directivity and cross-pol characteristics in the loop radiation was also achieved.

However, it is found in [17] that though the characteristics of an isolated loop antenna are significantly enhanced while radiating around a conducting cone, the same could only be achieved for a loop antenna located above the cone tip by using a parasitic loop. The placement of the loop antenna above the cone tip might be significant for many practical antenna structures with the height of the antenna above the ground being an important factor that strongly affects its performance with respect to the efficiency of signal transmission/reception and reduced electromagnetic interference and radio-frequency (RF) exposure to neighbouring areas. An alternate strategy to solve this is proposed in the current work by loading the cone tip with a spherical cap. As a result, the matching and interaction of the loop with the cone tip is significantly enhanced for the loop antenna located above the cone

tip. In addition, the design parameters can be suitably altered to achieve an impedance match for a wide range of loop radius and loop location, thus enhancing the practical utility and versatility of the design. A higher degree of freedom is also obtained for the antenna radius and vertical location for the loop antenna above the cone tip in the current configuration than for the loop antenna around the cone body in [17] due to the presence of the conducting cone body inside the loop for the latter case. It might also be noted that even with the use of a second parasitic loop for matching the loop antenna over the cone tip in [17], matching can be achieved for specific loop radius and locations of the primary loop only. In addition, the parasitic loop radius and location has to be changed to obtain match whenever the radius and location of the primary loop antenna changes. In comparison, the spherical cap over the cone tip can be designed for obtaining match over a wide range of dimensions and locations of the primary loop antenna. The dimension of the spherical cap is also fixed over a range of radius and locations of the loop antenna and needs to be changed only beyond this range. The effect of an adjacent loop placed in the vicinity of the primary loop for the current configuration is also investigated.

The antenna structure can be practically useful for antennas that need to be mounted high above the ground over conical roof tops or over the nose cone of airborne vehicles including aircrafts, rockets or missiles or high-speed land vehicles including automobiles and rail systems. For such vehicular applications, the placement of the loop above the cone tip helps in reduction of interference and scattering from the vehicle body. The structure can also be deployed in collision–avoidance systems in land and airborne vehicles. The frequency range of 1–6 GHz used in the investigation covers the L, S and part of the C band. This frequency band is typically used for sensor network communication. The investigation also covers the 8–12 GHz (X-band) that is typically used for defence and military applications. It is observed that the vicinity of the conical structure with the spherical cap can significantly alter the electrical characteristics of the loop antenna.

A full-wave analysis is also conducted for the proposed composite antenna configuration consisting of the spherical and conical shapes considering all eigenmodes of the structure. It might also be noted that though the dyadic Green's function for the structure is given in [18], the formulation based on the dyadic
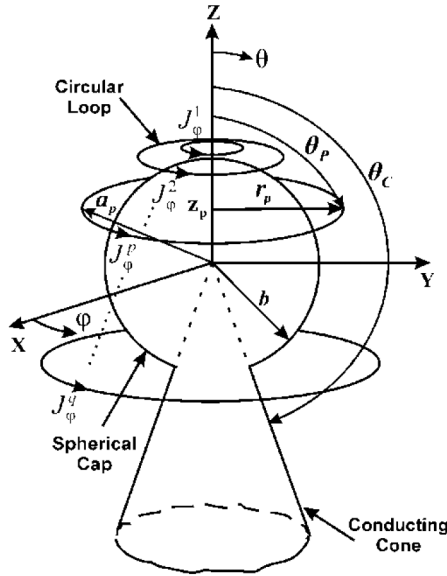
$$F_{\mathrm{r}} = \sum_m \sum_\mu P_\mu^m(\cos\theta)\begin{pmatrix}\sin(m\phi)\\\cos(m\phi)\end{pmatrix}$$

$$\times\begin{vmatrix}\begin{pmatrix}E_{m\mu}^0\\F_{m\mu}^0\end{pmatrix}\hat{H}_\mu^{(1)}(kr) + \begin{pmatrix}G_{m\mu}^0\\H_{m\mu}^0\end{pmatrix}\hat{H}_\mu^{(2)}(kr) \quad\text{for } b < r < a_1\\[1em]\begin{pmatrix}E_{m\mu}^p\\F_{m\mu}^p\end{pmatrix}\hat{H}_\mu^{(1)}(kr) + \begin{pmatrix}G_{m\mu}^p\\H_{m\mu}^p\end{pmatrix}\hat{H}_\mu^{(2)}(kr) \quad\text{for } a_p < r < a_{p+1}\\[1em]\begin{pmatrix}G_{m\mu}^q\\H_{m\mu}^q\end{pmatrix}\hat{H}_\mu^{(2)}(kr) \quad\qquad\text{for } r > a_q\end{vmatrix} \quad(1b)$$

In the above, $A_{m\nu}^p$, $B_{m\nu}^p$, $C_{m\nu}^p$, $D_{m\nu}^p$, $E_{m\mu}^p$, $F_{m\mu}^p$, $G_{m\mu}^p$ and $H_{m\mu}^p$ refer to the unknown potential coefficients. $P_l^m(x)$ ($l = \nu, \mu$) are associated Legendre functions of the first kind with order m and degree l. $\hat{H}_l^{(1)}(x)$ and $\hat{H}_l^{(2)}(x)$ ($l = \nu, \mu$) are, respectively, the spherical Hankel functions of the first and second kinds (Schelkunoff type) of order l. All other symbols have the usual meanings. The electric and magnetic fields can be obtained from (1a) and (1b) [19].

In addition to the boundary condition on the surface of the cone [17], the boundary condition corresponding to the tangential electric field should be enforced on the surface of the spherical cap. The tangential electric field E_ϕ at $r = b$ is given by

$$E_\phi(r = b) = \frac{1}{j\omega\epsilon b \sin\theta}\sum_m\sum_\nu k\left\{\begin{pmatrix}A_{m\nu}^0\\B_{m\nu}^0\end{pmatrix}\hat{H}_\nu^{(1)'}(kb)\right.$$
$$+\left.\begin{pmatrix}C_{m\nu}^0\\D_{m\nu}^0\end{pmatrix}\hat{H}_\nu^{(2)'}(kb)\right\}P_\nu^m(\cos\theta)\begin{pmatrix}m\cos(m\phi)\\-m\sin(m\phi)\end{pmatrix}$$
$$+\frac{1}{r}\sum_m\sum_\mu\left\{\begin{pmatrix}E_{m\mu}^0\\F_{m\mu}^0\end{pmatrix}\hat{H}_\mu^{(1)}(kb)\right.$$
$$+\left.\begin{pmatrix}G_{m\mu}^0\\H_{m\mu}^0\end{pmatrix}\hat{H}_\mu^{(2)}(kb)\right\}\frac{d}{d\theta}\left(P_\mu^m(\cos\theta)\right)\begin{pmatrix}\sin(m\phi)\\\cos(m\phi)\end{pmatrix} = 0 \quad(2)$$

From (2), the following two conditions are additionally enforced corresponding to the transverse magnetic (TM) and transverse electric (TE) modes:

$$\begin{pmatrix}A_{m\nu}^0\\B_{m\nu}^0\end{pmatrix}\hat{H}_\nu^{(1)'}(kb) + \begin{pmatrix}C_{m\nu}^0\\D_{m\nu}^0\end{pmatrix}\hat{H}_\nu^{(2)'}(kb) = 0 \quad(3)$$

for the TM to r mode

$$\begin{pmatrix}E_{m\mu}^0\\F_{m\mu}^0\end{pmatrix}\hat{H}_\mu^{(1)}(kb) + \begin{pmatrix}G_{m\mu}^0\\H_{m\mu}^0\end{pmatrix}\hat{H}_\mu^{(2)}(kb) = 0 \quad(4)$$

for the TE to r mode.

The magnetic and the electric vector potentials for $b < r < a_1$ can, therefore, be written as

$$A_r = \sum_m\sum_\nu\begin{pmatrix}A_{m\nu}^0\\B_{m\nu}^0\end{pmatrix}P_\nu^m(\cos\theta)\begin{pmatrix}\sin(m\phi)\\\cos(m\phi)\end{pmatrix}$$
$$\left\{\hat{H}_\nu^{(1)}(kr) - \frac{\hat{H}_\nu^{(1)'}(kb)}{\hat{H}_\nu^{(2)'}(kb)}\hat{H}_\nu^{(2)}(kr)\right\} \quad(5a)$$

and

$$F_r = \sum_m\sum_\mu\begin{pmatrix}E_{m\mu}^0\\F_{m\mu}^0\end{pmatrix}P_\mu^m(\cos\theta)\begin{pmatrix}\sin(m\phi)\\\cos(m\phi)\end{pmatrix}$$
$$\left\{\hat{H}_\mu^{(1)}(kr) - \frac{\hat{H}_\mu^{(1)'}(kb)}{\hat{H}_\mu^{(2)'}(kb)}\hat{H}_\mu^{(2)}(kr)\right\} \quad(5b)$$

Fig. 1 *Antenna configuration with loop antennas above and around a conducting cone with a spherical cap*

Green's function works with all field components simultaneously leading to an increased computational burden. The current formulation using the scalar Green's function approach for the treatment of the composite structure is distinctly different from [18], in which only the relevant field components needed in the formulation can be efficiently computed, without computation of the other field components.

The reflection coefficient and radiation pattern of the loop antenna in the proximity of the composite structure are evaluated. The mutual coupling between adjacent loops is characterised to evaluate the effect of a parasitic loop on the matching characteristics of the primary excited loop in the presence of the composite structure. An excellent agreement is observed between the computed, simulated and measured results.

2 Analysis of the antenna structure

The antenna configuration is shown in Fig. 1. The cone vertex is located at the origin of the spherical coordinate system with a conducting spherical cap of radius b over the cone with the centre of the cap coinciding with the cone vertex. The loop antenna configuration is placed around the cone of exterior angle θ_c. The total number of loops is denoted by q. The pth loop is located at $r = a_p$ and at an elevation angle $\theta = \theta_p$, with the ϕ-directed loop current on the pth loop denoted by J_ϕ^p. The electric and magnetic fields for the composite antenna structure consisting of the spherical cap loaded conducting cone can be derived from the magnetic and electric vector potentials A_r and F_r, respectively, given as follows:

$$A_r = \sum_m\sum_\nu P_\nu^m(\cos\theta)\begin{pmatrix}\sin(m\phi)\\\cos(m\phi)\end{pmatrix}$$

$$\times\begin{vmatrix}\begin{pmatrix}A_{m\nu}^0\\B_{m\nu}^0\end{pmatrix}\hat{H}_\nu^{(1)}(kr) + \begin{pmatrix}C_{m\nu}^0\\D_{m\nu}^0\end{pmatrix}\hat{H}_\nu^{(2)}(kr) \quad\text{for } b < r < a_1\\[1em]\begin{pmatrix}A_{m\nu}^p\\B_{m\nu}^p\end{pmatrix}\hat{H}_\nu^{(1)}(kr) + \begin{pmatrix}C_{m\nu}^p\\D_{m\nu}^p\end{pmatrix}\hat{H}_\nu^{(2)}(kr) \quad\text{for } a_p < r < a_{p+1}\\[1em]\begin{pmatrix}C_{m\nu}^q\\D_{m\nu}^q\end{pmatrix}\hat{H}_\nu^{(2)}(kr) \quad\qquad\text{for } r > a_q\end{vmatrix} \quad(1a)$$

To find the unknown coefficients in (1a) and (1b), the boundary conditions for the tangential field components E_θ, E_ϕ, H_θ and H_ϕ are applied on the loop. Equating E_θ at $r = a_1^-$ and $r = a_1^+$, multiplying both sides first by $\cos(l\phi)$ and then by $\sin(l\phi)$ and integrating from 0 to 2π to eliminate the summation over m, we obtain the following two equations:

$$\frac{k}{j\omega\varepsilon} \sum_\nu B_{m\nu}^0 \left\{ \hat{H}_\nu^{(1)'}(ka_1) - \frac{\hat{H}_\nu^{(1)'}(kb)}{\hat{H}_\nu^{(2)'}(kb)} \hat{H}_\nu^{(2)'}(ka_1) \right\} \frac{d}{d\theta}(P_\nu^m(\cos\theta))$$

$$-\frac{m}{\sin\theta} \sum_\mu E_{m\mu}^0 \left\{ \hat{H}_\mu^{(1)}(ka_1) - \frac{\hat{H}_\mu^{(1)}(kb)}{\hat{H}_\mu^{(2)}(kb)} \hat{H}_\mu^{(2)}(ka_1) \right\} P_\mu^m(\cos\theta) \quad (6a)$$

$$= \frac{k}{j\omega\varepsilon} \sum_\nu \left\{ B_{m\nu}^1 \hat{H}_\nu^{(1)'}(ka_1) + D_{m\nu}^1 \hat{H}_\nu^{(2)'}(ka_1) \right\} \frac{d}{d\theta}(P_\nu^m(\cos\theta))$$

$$-\frac{m}{\sin\theta} \sum_\mu \left\{ E_{m\mu}^1 \hat{H}_\mu^{(1)}(ka_1) + G_{m\mu}^1 \hat{H}_\mu^{(2)}(ka_1) \right\} P_\mu^m(\cos\theta)$$

$$\frac{k}{j\omega\varepsilon} \sum_\nu A_{m\nu}^0 \left\{ \hat{H}_\nu^{(1)'}(ka_1) - \frac{\hat{H}_\nu^{(1)'}(kb)}{\hat{H}_\nu^{(2)'}(kb)} \hat{H}_\nu^{(2)'}(ka_1) \right\} \frac{d}{d\theta}(P_\nu^m(\cos\theta))$$

$$+\frac{m}{\sin\theta} \sum_\mu F_{m\mu}^0 \left\{ \hat{H}_\mu^{(1)}(ka_1) - \frac{\hat{H}_\mu^{(1)}(kb)}{\hat{H}_\mu^{(2)}(kb)} \hat{H}_\mu^{(2)}(ka_1) \right\} P_\mu^m(\cos\theta)$$

$$= \frac{k}{j\omega\varepsilon} \sum_\nu \left\{ A_{m\nu}^1 \hat{H}_\nu^{(1)'}(ka_1) + C_{m\nu}^1 \hat{H}_\nu^{(2)'}(ka_1) \right\} \frac{d}{d\theta}(P_\nu^m(\cos\theta)) \quad (6b)$$

$$+\frac{m}{\sin\theta} \sum_\mu \left\{ F_{m\mu}^1 \hat{H}_\mu^{(1)}(ka_1) + H_{m\mu}^1 \hat{H}_\mu^{(2)}(ka_1) \right\} P_\mu^m(\cos\theta)$$

$$(m \neq 0)$$

Using the continuity of E_ϕ at $r = a_1$ and performing a similar operation yields:

$$\frac{mk}{j\omega\varepsilon\sin\theta} \sum_\nu A_{m\nu}^0 \left\{ \hat{H}_\nu^{(1)'}(ka_1) - \frac{\hat{H}_\nu^{(1)'}(kb)}{\hat{H}_\nu^{(2)'}(kb)} \hat{H}_\nu^{(2)'}(ka_1) \right\} P_\nu^m(\cos\theta)$$

$$+ \sum_\mu F_{m\mu}^0 \left\{ \hat{H}_\mu^{(1)}(ka_1) - \frac{\hat{H}_\mu^{(1)}(kb)}{\hat{H}_\mu^{(2)}(kb)} \hat{H}_\mu^{(2)}(ka_1) \right\} \frac{d}{d\theta}(P_\mu^m(\cos\theta)) \quad (7a)$$

$$= \frac{mk}{j\omega\varepsilon\sin\theta} \sum_\nu \left\{ A_{m\nu}^1 \hat{H}_\nu^{(1)'}(ka_1) + C_{m\nu}^1 \hat{H}_\nu^{(2)'}(ka_1) \right\} P_\nu^m(\cos\theta)$$

$$+ \sum_\mu \left\{ F_{m\mu}^1 \hat{H}_\mu^{(1)}(ka_1) + H_{m\mu}^1 \hat{H}_\mu^{(2)}(ka_1) \right\} \frac{d}{d\theta}(P_\mu^m(\cos\theta))$$

and

$$-\frac{mk}{j\omega\varepsilon\sin\theta} \sum_\nu B_{m\nu}^0 \left\{ \hat{H}_\nu^{(1)'}(ka_1) - \frac{\hat{H}_\nu^{(1)'}(kb)}{\hat{H}_\nu^{(2)'}(kb)} \hat{H}_\nu^{(2)'}(ka_1) \right\} P_\nu^m(\cos\theta)$$

$$+ \sum_\mu E_{m\mu}^0 \left\{ \hat{H}_\mu^{(1)}(ka_1) - \frac{\hat{H}_\mu^{(1)}(kb)}{\hat{H}_\mu^{(2)}(kb)} \hat{H}_\mu^{(2)}(ka_1) \right\} \frac{d}{d\theta}(P_\mu^m(\cos\theta)) \quad (7b)$$

$$= -\frac{mk}{j\omega\varepsilon\sin\theta} \sum_\nu \left\{ B_{m\nu}^1 \hat{H}_\nu^{(1)'}(ka_1) + D_{m\nu}^p \hat{H}_\nu^{(2)'}(ka_1) \right\} P_\nu^m(\cos\theta)$$

$$+ \sum_\mu \left\{ E_{m\mu}^0 \hat{H}_\mu^{(1)}(ka_1) + G_{m\mu}^p \hat{H}_\mu^{(2)}(ka_1) \right\} \frac{d}{d\theta}(P_\mu^m(\cos\theta))$$

$$(m \neq 0)$$

To eliminate the summation over ν, we multiply (6a) by $\sin\theta$, differentiate with respect to θ and add the result with $m \times (7b)$ to yield

$$\sum_\nu B_{m\nu}^0 \left\{ \hat{H}_\nu^{(1)'}(ka_1) - \frac{\hat{H}_\nu^{(1)'}(kb)}{\hat{H}_\nu^{(2)'}(kb)} \hat{H}_\nu^{(2)'}(ka_1) \right\}$$

$$\left\{ \frac{d}{d\theta}\left(\sin\theta\frac{d}{d\theta}(P_\nu^m(\cos\theta))\right) - \frac{m^2}{\sin\theta}P_\nu^m(\cos\theta) \right\}$$

$$= \sum_\nu \left\{ B_{m\nu}^1 \hat{H}_\nu^{(1)'}(ka_1) + D_{m\nu}^1 \hat{H}_\nu^{(2)'}(ka_1) \right\} \quad (8)$$

$$\left\{ \frac{d}{d\theta}\left(\sin\theta\frac{d}{d\theta}(P_\nu^m(\cos\theta))\right) - \frac{m^2}{\sin\theta}P_\nu^m(\cos\theta) \right\}$$

$$(m \neq 0)$$

Using the associated Legendre equation

$$\frac{d}{d\theta}\left(\sin\theta\frac{d}{d\theta}(P_\nu^m(\cos\theta))\right) - \frac{m^2}{\sin\theta}P_\nu^m(\cos\theta)$$

$$= -\nu(\nu+1)\sin\theta P_\nu^m(\cos\theta) \quad (9)$$

multiplying both sides of (8) by $P_\lambda^m(\cos\theta)$, where $P_\lambda^m(\cos\theta_c) = 0$ and integrating from 0 to θ_c produces

$$B_{m\nu}^0 \left\{ \hat{H}_\nu^{(1)'}(ka_1) - \frac{\hat{H}_\nu^{(1)'}(kb)}{\hat{H}_\nu^{(2)'}(kb)} \hat{H}_\nu^{(2)'}(ka_1) \right\}$$

$$-B_{m\nu}^1 \hat{H}_\nu^{(1)'}(ka_1) - D_{m\nu}^1 \hat{H}_\nu^{(2)'}(ka_1) = 0 \quad (m \neq 0) \quad (10)$$

Similarly, (7a) is multiplied by m. The resultant equation is subtracted from the equation obtained by multiplying (6b) by $\sin\theta$ and differentiating with respect to θ. Next, following similar steps used as before for (10), we obtain:

$$A_{m\nu}^0 \left\{ \hat{H}_\nu^{(1)'}(ka_1) - \frac{\hat{H}_\nu^{(1)'}(kb)}{\hat{H}_\nu^{(2)'}(kb)} \hat{H}_\nu^{(2)'}(ka_1) \right\}$$

$$-A_{m\nu}^1 \hat{H}_\nu^{(1)'}(ka_1) - C_{m\nu}^1 \hat{H}_\nu^{(2)'}(ka_1) = 0 \quad (m \neq 0) \quad (11)$$

The two corresponding equations for TE modes generated using the above procedure are given as follows:

$$E_{m\mu}^0 \left\{ \hat{H}_\mu^{(1)}(ka_1) - \frac{\hat{H}_\mu^{(1)}(kb)}{\hat{H}_\mu^{(2)}(kb)} \hat{H}_\mu^{(2)}(ka_1) \right\}$$

$$-E_{m\mu}^1 \hat{H}_\mu^{(1)}(ka_1) - G_{m\mu}^1 \hat{H}_\mu^{(2)}(ka_1) = 0 \quad (m \neq 0) \quad (12)$$

$$F_{m\mu}^0 \left\{ \hat{H}_\mu^{(1)}(ka_1) - \frac{\hat{H}_\mu^{(1)}(kb)}{\hat{H}_\mu^{(2)}(kb)} \hat{H}_\mu^{(2)}(ka_1) \right\}$$

$$-F_{m\mu}^1 \hat{H}_\mu^{(1)}(ka_1) - H_{m\mu}^1 \hat{H}_\mu^{(2)}(ka_1) = 0 \quad (m \neq 0) \quad (13)$$

Performing similar operations on the continuity equations for the magnetic field over the first loop

$$H_\theta(r = a_1^-) - H_\theta(r = a_1^+) = -J_\phi^1 \quad (14a)$$

$$H_\phi(r = a_1^-) = H_\phi(r = a_1^+) \quad (14b)$$

we obtain the following four equations:

$$A_{m\nu}^0 \left\{ \hat{H}_\nu^{(1)}(ka_1) - \frac{\hat{H}_\nu^{(1)'}(kb)}{\hat{H}_\nu^{(2)'}(kb)} \hat{H}_\nu^{(2)}(ka_1) \right\}$$

$$-A_{m\nu}^1 \hat{H}_\nu^{(1)}(ka_1) - C_{m\nu}^1 \hat{H}_\nu^{(2)}(ka_1)$$

$$= -\frac{ma_1}{\pi\nu(\nu+1)I_{m\nu}} \int_0^{\theta_c} P_\nu^m(\cos\theta) \int_0^{2\pi} J_\phi^1 \cos(m\phi)d\phi d\theta \quad (15)$$

$$(m \neq 0)$$

2561

where $I_{m\nu} = \dfrac{1}{(2\nu + 1)}\left[\sin\theta \dfrac{\mathrm{d}P_\nu^m(\cos\theta)}{\mathrm{d}\theta} \dfrac{\mathrm{d}P_\nu^m(\cos\theta)}{\mathrm{d}\nu}\right]_{\theta = \theta_c}$

$$B_{m\nu}^0\left\{\hat{H}_\nu^{(1)}(ka_1) - \dfrac{\hat{H}_\nu^{(1)\prime}(kb)}{\hat{H}_\nu^{(2)\prime}(kb)}\hat{H}_\nu^{(2)}(ka_1)\right\}$$
$$- B_{m\nu}^1\hat{H}_\nu^{(1)}(ka_1) - D_{m\nu}^1\hat{H}_\nu^{(2)}(ka_1)$$
$$= \dfrac{ma_1}{\pi\nu(\nu + 1)I_{m\nu}}\int_0^{\theta_c} P_\nu^m(\cos\theta)\int_0^{2\pi} J_\phi^1\sin(m\phi)\mathrm{d}\phi\,\mathrm{d}\theta \tag{16}$$
$$(m \neq 0)$$

$$F_{m\mu}^0\left\{\hat{H}_\mu^{(1)\prime}(ka_1) - \dfrac{\hat{H}_\mu^{(1)}(kb)}{\hat{H}_\mu^{(2)}(kb)}\hat{H}_\mu^{(2)\prime}(ka_1)\right\}$$
$$- F_{m\mu}^1\hat{H}_\mu^{(1)\prime}(ka_1) - H_{m\mu}^1\hat{H}_\mu^{(2)\prime}(ka_1)$$
$$= \dfrac{j\eta a_1}{\pi\mu(\mu + 1)I_{m\mu}}\int_0^{\theta_c} P_\mu^m(\cos\theta)\dfrac{d}{d\theta}\left(\sin\theta\int_0^{2\pi} J_\phi^1\cos(m\phi)\mathrm{d}\phi\right)\mathrm{d}\theta \tag{17}$$
$$(m \neq 0)$$

where $I_{m\mu} = -\dfrac{1}{(2\mu + 1)}\left[\sin\theta P_\mu^m(\cos\theta)\dfrac{d^2 P_\mu^m(\cos\theta)}{d\theta\,d\mu}\right]_{\theta = \theta_c}$

$$E_{m\mu}^0\left\{\hat{H}_\mu^{(1)\prime}(ka_1) - \dfrac{\hat{H}_\mu^{(1)}(kb)}{\hat{H}_\mu^{(2)}(kb)}\hat{H}_\mu^{(2)\prime}(ka_1)\right\}$$
$$- E_{m\mu}^1\hat{H}_\mu^{(1)\prime}(ka_1) - G_{m\mu}^1\hat{H}_\mu^{(2)\prime}(ka_1)$$
$$= \dfrac{j\eta a_1}{\pi\mu(\mu + 1)I_{m\mu}}\int_0^{\theta_c} P_\mu^m(\cos\theta)\dfrac{d}{d\theta}\left(\sin\theta\int_0^{2\pi} J_\phi^1\sin(m\phi)\mathrm{d}\phi\right)\mathrm{d}\theta \tag{18}$$
$$(m \neq 0)$$

Eight equations similar to the above can be obtained by matching the boundary conditions over the pth loop. They are not repeated for the sake of brevity.

To evaluate the potential constants for $m = 0$, (6a) is multiplied by $\sin\theta$ and differentiated with respect to θ to produce

$$\sum_\nu B_{0\nu}^0\left\{\hat{H}_\nu^{(1)\prime}(ka_1) - \dfrac{\hat{H}_\nu^{(1)\prime}(kb)}{\hat{H}_\nu^{(2)\prime}(kb)}\hat{H}_\nu^{(2)}(ka_1)\right\}$$
$$\dfrac{d}{d\theta}\left(\sin\theta\dfrac{d}{d\theta}(P_\nu(\cos\theta))\right)$$
$$= \sum_\nu\left\{B_{0\nu}^1\hat{H}_\nu^{(1)\prime}(ka_1) + D_{0\nu}^1\hat{H}_\nu^{(2)\prime}(ka_1)\right\}$$
$$\dfrac{d}{d\theta}\left(\sin\theta\dfrac{d}{d\theta}(P_\nu(\cos\theta))\right) \tag{19}$$

Next, using the same procedure as in (10) we get

$$B_{0\nu}^0\left\{\hat{H}_\nu^{(1)\prime}(ka_1) - \dfrac{\hat{H}_\nu^{(1)\prime}(kb)}{\hat{H}_\nu^{(2)\prime}(kb)}\hat{H}_\nu^{(2)}(ka_1)\right\}$$
$$- B_{0\nu}^1\hat{H}_\nu^{(1)\prime}(ka_1) - D_{0\nu}^1\hat{H}_\nu^{(2)\prime}(ka_1) = 0 \tag{20}$$

A similar operation is performed in (7a), which yields the following:

$$F_{0\mu}^0\left\{\hat{H}_\mu^{(1)}(ka_1) - \dfrac{\hat{H}_\mu^{(1)}(kb)}{\hat{H}_\mu^{(2)}(kb)}\hat{H}_\mu^{(2)}(ka_1)\right\}$$
$$- F_{0\mu}^1\hat{H}_\mu^{(1)}(ka_1) - H_{0\mu}^1\hat{H}_\mu^{(2)}(ka_1) = 0 \tag{21}$$

Two corresponding equations are also produced from the magnetic field continuity equations (14a) and (14b) for $m = 0$ as follows:

$$B_{0\nu}^0\left\{\hat{H}_\nu^{(1)}(ka_1) - \dfrac{\hat{H}_\nu^{(1)\prime}(kb)}{\hat{H}_\nu^{(2)\prime}(kb)}\hat{H}_\nu^{(2)}(ka_1)\right\}$$
$$- B_{0\nu}^1\hat{H}_\nu^{(1)}(ka_1) - D_{0\nu}^1\hat{H}_\nu^{(2)}(ka_1) = 0 \tag{22}$$

$$F_{0\mu}^0\left\{\hat{H}_\mu^{(1)\prime}(ka_1) - \dfrac{\hat{H}_\mu^{(1)}(kb)}{\hat{H}_\mu^{(2)}(kb)}\hat{H}_\mu^{(2)\prime}(ka_1)\right\}$$
$$- F_{0\mu}^1\hat{H}_\mu^{(1)\prime}(ka_1) - H_{0\mu}^1\hat{H}_\mu^{(2)\prime}(ka_1)$$
$$= \dfrac{j\eta a_1}{2\pi\mu(\mu + 1)I_{0\mu}}\int_0^{\theta_c} P_\mu(\cos\theta)\dfrac{d}{d\theta}\left(\sin\theta\int_0^{2\pi} J_\phi^1\mathrm{d}\phi\right)\mathrm{d}\theta \tag{23}$$

The current J_ϕ^p on the pth loop in the above can be expressed as follows, using the thin-loop approximation:

$$J_\phi^p = \dfrac{1}{a_p}\sum_{m'=0}^\infty I_{m'}^p\cos(m'\phi)\delta(\theta - \theta_p) \tag{24}$$

where $I_{m'}^p$ are the unknown current harmonics and $\delta(\theta)$ is the Dirac-delta function.

Using (24), the right-hand side (RHS) of (16) and (18) can be evaluated to be zero while that of (15) is given by

$$U_{m\nu}^1 = -\dfrac{mI_m^1}{\nu(\nu + 1)I_{m\nu}}P_\nu^m(\cos\theta_1) \qquad (m \neq 0) \tag{25}$$

For (17), (23), using (24) the RHS can be evaluated to be

$$V_{m\mu}^1 = -\dfrac{jI_m^1}{\mu(\mu + 1)I_{m\mu}}\sin\theta_1\left[\dfrac{d}{d\theta}\left(P_\mu^m(\cos\theta)\right)\right]_{\theta = \theta_1}(\forall m) \tag{26}$$

Using (10), (12), (16), (20), (22) and (18), it is observed that $B_{m\nu}^0 = B_{m\nu}^1 = D_{m\nu}^1 = 0$ ($\forall m$) and $E_{m\mu}^0 = E_{m\mu}^1 = G_{m\mu}^1 = 0$ ($m \neq 0$). To compute the constants $A_{m\nu}^0$, $A_{m\nu}^1$ and $C_{m\nu}^1$ ($m \neq 0$), (11) is multiplied by $\hat{H}_\nu^{(2)}(ka_1)$. The result is subtracted from (15) $\times \hat{H}_\nu^{(2)}(ka_1)$. Next, using the Wronskian relationship

$$\hat{H}_\nu^{(1)}(ka_1)\hat{H}_\nu^{(2)\prime}(ka_1) - \hat{H}_\nu^{(1)\prime}(ka_1)\hat{H}_\nu^{(2)}(ka_1) = -2j \tag{27}$$

yields

$$2A_{m\nu}^0 - 2A_{m\nu}^1 = jU_{m\nu}^1\hat{H}_\nu^{(2)\prime}(ka_1) \tag{28}$$

The following equation can also be derived in a similar manner from (11) and (15), using (27):

$$\zeta'A_{m\nu}^0 - 2C_{m\nu}^1 = -jU_{m\nu}^1\hat{H}_\nu^{(1)\prime}(ka_1) \tag{29}$$

where $\zeta' = -2\dfrac{\hat{H}_\nu^{(1)\prime}(kb)}{\hat{H}_\nu^{(2)\prime}(kb)}$. Following the above procedure, the four sets of equations below (30)–(33) can also be derived for the intermediate (pth) and last loops, using (27):

$$2A_{m\nu}^{p-1} - 2A_{m\nu}^p = jU_{m\nu}^p\hat{H}_\nu^{(2)\prime}(ka_p) \qquad \text{(for the } p\text{th loop)} \tag{30}$$

$$2A_{m\nu}^{p-1} - 2C_{m\nu}^p = -jU_{m\nu}^p\hat{H}_\nu^{(1)\prime}(ka_p) \qquad \text{(for the } p\text{th loop)} \tag{31}$$

$$2A_{m\nu}^{q-1} = jU_{m\nu}^q\hat{H}_\nu^{(2)\prime}(ka_q) \qquad \text{(for the } q\text{th loop)} \tag{32}$$

$$2C_{m\nu}^{q-1} - 2C_{m\nu}^q = -jU_{m\nu}^q \hat{H}_\nu^{(1)\prime}(ka_q) \quad \text{(for the } q\text{th loop)} \quad (33)$$

From (28)–(33), the constants $A_{m\nu}^l$ and $C_{m\nu}^k$ are evaluated as

$$[A_{m\nu}^0, \ldots, A_{m\nu}^{q-1}, C_{m\nu}^1, \ldots, C_{m\nu}^q]^{\mathrm{T}} = [P_{m\nu}][I_m] \quad (34)$$

where

$$[P_{m\nu}] = [X]^{-1}[U'_{m\nu}] \quad (35)$$

(see (36))

$$[U'_{m\nu}] = \mathrm{diag}
\begin{bmatrix}
\hat{H}_\nu^{(2)\prime}(ka_1)U_{m\nu}^{\prime 1} \\
-\hat{H}_\nu^{(1)\prime}(ka_1)U_{m\nu}^{\prime 1} \\
\vdots \\
\hat{H}_\nu^{(2)\prime}(ka_p)U_{m\nu}^{\prime p} \\
-\hat{H}_\nu^{(1)\prime}(ka_p)U_{m\nu}^{\prime p} \\
\vdots \\
\hat{H}_\nu^{(2)\prime}(ka_q)U_{m\nu}^{\prime q} \\
-\hat{H}_\nu^{(1)\prime}(ka_q)U_{m\nu}^{\prime q}
\end{bmatrix}, \quad U_{m\nu}^{\prime p} = jU_{m\nu}^p/I_m^p \quad (37)$$

and

$$[I_m] = [I_m^1\ I_m^1\ \ldots\ I_m^q\ I_m^q]^{\mathrm{T}} \quad (38)$$

Similarly, the constants $F_{m\mu}^l$ and $H_{m\mu}^k$ are evaluated as

$$[F_{m\mu}^0, \ldots, F_{m\mu}^{q-1}, H_{m\mu}^1, \ldots, H_{m\mu}^q]^{\mathrm{T}} = [Q_{m\mu}][I_m] \quad (39)$$

where

$$[Q_{m\mu}] = [Y]^{-1}[V'_{m\mu}] \quad (40)$$

with

(see (41))

with $\zeta = -2\dfrac{\hat{H}_\mu^{(1)}(kb)}{\hat{H}_\mu^{(2)}(kb)}$

$$[V'_{m\mu}] = \mathrm{diag}
\begin{bmatrix}
-\hat{H}_\mu^{(2)}(ka_1)V_{m\mu}^{\prime 1} \\
\hat{H}_\mu^{(1)}(ka_1)V_{m\mu}^{\prime 1} \\
\vdots \\
-\hat{H}_\mu^{(2)}(ka_p)V_{m\mu}^{\prime p} \\
\hat{H}_\mu^{(1)}(ka_p)V_{m\mu}^{\prime p} \\
\vdots \\
-\hat{H}_\mu^{(2)}(ka_q)V_{m\mu}^{\prime q} \\
\hat{H}_\mu^{(2)}(ka_q)V_{m\mu}^{\prime q}
\end{bmatrix}, \quad V_{m\mu}^{\prime p} = jV_{m\mu}^p/I_m^p \quad (42)$$

Now, using the expression for the scattered field $E_\phi(a_i, \theta'_i, \phi)$ and enforcing that the tangential electric field vanishes on the surface of the ith loop, we obtain

$$\frac{k}{j\omega\varepsilon}\sum_m\sum_\nu \left\{ A_{m\nu}^i \hat{H}_\nu^{(1)\prime}(ka_i) + C_{m\nu}^i \hat{H}_\nu^{(2)\prime}(ka_i) \right\}$$

$$m\cos(m\phi)P_\nu^m(\cos\theta'_i)$$

$$+\sin\theta'_i \sum_m\sum_\mu \left\{ F_{m\mu}^i \hat{H}_\mu^{(1)}(ka_i) + H_{m\mu}^i \hat{H}_\mu^{(2)}(ka_i) \right\}$$

$$\cos(m\phi)\frac{d}{d\theta}(P_\mu^m(\cos\theta))_{\theta=\theta'_i} = -V_i\delta(\phi)$$

$$(43)$$

where

$$\theta'_i = \theta_i - \tan^{-1}\left(\frac{w_i}{a_i}\right) \quad (44)$$

with a_i being the radius of the ith loop; w_i the wire radius; and V_i the impressed voltage on the ith loop.

Multiplying (43) by $\cos(l\phi)$ and integrating from 0 to 2π and using (34) and (39), we obtain

$$\sum_{p=1}^q Z_m^{ip} I_m^p = -\frac{V_i}{(1+\delta_{m0})\pi} \quad (45)$$

where

$$[X] =
\begin{bmatrix}
2 & -2 & \cdots & 0 & 0 & \cdots & 0 & 0 & \cdots & 0 & 0 & \cdots & 0 & 0 \\
\zeta' & 0 & \cdots & 0 & 0 & \cdots & 0 & -2 & \cdots & 0 & 0 & \cdots & 0 & 0 \\
\vdots & \vdots & \cdots & \vdots & \vdots & \cdots & \vdots & \vdots & \cdots & \vdots & \vdots & \cdots & \vdots & \vdots \\
0 & 0 & \cdots & 2 & -2 & \cdots & 0 & 0 & \cdots & 0 & 0 & \cdots & 0 & 0 \\
0 & 0 & \cdots & 0 & 0 & \cdots & 0 & 0 & \cdots & 2 & -2 & \cdots & 0 & 0 \\
\vdots & \vdots & \cdots & \vdots & \vdots & \cdots & \vdots & \vdots & \cdots & \vdots & \vdots & \cdots & \vdots & \vdots \\
0 & 0 & \cdots & 0 & 0 & \cdots & 2 & 0 & \cdots & 0 & 0 & \cdots & 0 & 0 \\
0 & 0 & \cdots & 0 & 0 & \cdots & 0 & 0 & \cdots & 0 & 0 & \cdots & 2 & -2
\end{bmatrix} \quad (36)$$

$$[Y] =
\begin{bmatrix}
2 & -2 & \cdots & 0 & 0 & \cdots & 0 & 0 & \cdots & 0 & 0 & \cdots & 0 & 0 \\
\zeta & 0 & \cdots & 0 & 0 & \cdots & 0 & -2 & \cdots & 0 & 0 & \cdots & 0 & 0 \\
\vdots & \vdots & \cdots & \vdots & \vdots & \cdots & \vdots & \vdots & \cdots & \vdots & \vdots & \cdots & \vdots & \vdots \\
0 & 0 & \cdots & 2 & -2 & \cdots & 0 & 0 & \cdots & 0 & 0 & \cdots & 0 & 0 \\
0 & 0 & \cdots & 0 & 0 & \cdots & 0 & 0 & \cdots & 2 & -2 & \cdots & 0 & 0 \\
\vdots & \vdots & \cdots & \vdots & \vdots & \cdots & \vdots & \vdots & \cdots & \vdots & \vdots & \cdots & \vdots & \vdots \\
0 & 0 & \cdots & 0 & 0 & \cdots & 2 & 0 & \cdots & 0 & 0 & \cdots & 0 & 0 \\
0 & 0 & \cdots & 0 & 0 & \cdots & 0 & 0 & \cdots & 0 & 0 & \cdots & 2 & -2
\end{bmatrix} \quad (41)$$

$$Z_m^{ip} = -j\eta \sum_\nu \left\{ \hat{H}_\nu^{(1)'}(ka_i)\left(P_{m\nu_{i+1},\,2p} + P_{m\nu_{i+1},\,2p-1}\right) \right.$$

$$+ \hat{H}_\nu^{(2)'}(ka_i)\left(P_{m\nu_{i+q},\,2p} + P_{m\nu_{i+q},\,2p-1}\right)\Big\} mP_\nu^m(\cos\theta'_i)$$

$$+ \sin\theta'_i \sum_\mu \left\{ \hat{H}_\mu^{(1)}(ka_i)\left(Q_{m\mu_{i+1},\,2p} + Q_{m\mu_{i+1},\,2p-1}\right) \right. \tag{46}$$

$$\left. + \hat{H}_\mu^{(2)}(ka_i)\left(Q_{m\mu_{i+q},\,2p} + Q_{m\mu_{i+q},\,2p-1}\right)\right\} \frac{d}{d\theta}\left(P_\mu^m(\cos\theta)\right)_{\theta=\theta'_i}$$

In (46), $P_{m\mu_{x,\,y}}$ and $Q_{m\mu_{x,\,y}}$ refer to the entries in the matrices $[\boldsymbol{P}_{m\nu}]$ and $[\boldsymbol{Q}_{m\mu}]$, respectively.

The unknown loop currents in the other loops can be obtained from

$$\begin{bmatrix} Z_m^{11} & Z_m^{12} & \cdots & Z_m^{1q} \\ Z_m^{21} & Z_m^{22} & \cdots & Z_m^{2q} \\ \vdots & \vdots & \ddots & \vdots \\ Z_m^{q1} & Z_m^{q2} & \cdots & Z_m^{qq} \end{bmatrix}\begin{bmatrix} I_m^1 \\ I_m^2 \\ \vdots \\ I_m^q \end{bmatrix} = \frac{-1}{(1+\delta_{m0})\pi}\begin{bmatrix} V_1 \\ V_2 \\ \vdots \\ V_q \end{bmatrix} \tag{47}$$

The radiated far-field components E_θ and E_ϕ are given by

$$E_\theta(r,\theta,\phi) = \frac{\eta}{jr}\sum_m\sum_\nu C_{m\nu}^q\hat{H}_\nu^{(2)'}(kr)\frac{d}{d\theta}(P_\nu^m(\cos\theta))\sin(m\phi)$$

$$+ \frac{1}{r\sin\theta}\sum_m\sum_\mu mH_{m\mu}^q\hat{H}_\mu^{(2)}(kr)P_\mu^m(\cos\theta)\sin(m\phi) \tag{48}$$

$$E_\phi(r,\theta,\phi) = \frac{\eta}{jr\sin\theta}\sum_m\sum_\nu mC_{m\nu}^q\hat{H}_\nu^{(2)'}(kr)P_\nu^m(\cos\theta)\cos(m\phi)$$

$$+ \frac{1}{r}\sum_m\sum_\mu H_{m\mu}^q\hat{H}_\mu^{(2)}(kr)\frac{d}{d\theta}(P_\mu^m(\cos\theta))\cos(m\phi) \tag{49}$$

The above full-wave technique considers all scattered higher-order modes in the formulation. In addition, compared to the finite element technique used for the analysis of conformal antennas on conical and spherical structures in [20], the above methodology avoids discretisation of the computational domain using volumetric elements that is a computationally intensive procedure. The method is also more efficient than the method of moment-based approach used in [21] for the analysis of scattering from a conducting conical shell that approximates the entire conical surface with triangular patch elements. This necessitates the determination of unknown induced currents on each patch that greatly increases the number of unknowns to be determined. The proposed technique is also advantageous over the finite difference time-domain-based (FDTD) approach used for the analysis of a biconical antenna in [22], with the conical surface approximated by a Yee FDTD mesh, together with an appropriate absorbing boundary condition for grid truncation with the fields evolving in a leap-frog time marching scheme. This needs considerable CPU time and memory overheads. The near-to-far-field transformation has to be also applied for computation of the far-field pattern and requires post-processing of the time-domain fields.

3 Results

The above formulation was used to evaluate the reflection coefficient of a loop antenna above the cone tip. It was also used to investigate the mutual coupling effect of a parasitic loop placed adjacent to the primary loop.

The reflection coefficient of a single-loop antenna above the cone tip with varying radius of the loop is shown in Fig. 2 and compared with an isolated loop antenna in free space. In this figure, the loop is located at a height of $z_1 = 2.1$ cm above the cone tip with an exterior angle of $\theta_c = 165°$ and a fixed spherical cap radius of $b = 1.5$ cm. The loop wire diameter is $d_w = 1$ mm, with an excitation voltage of 1 V at $\phi = 0°$. It is seen that the loop can be matched over a wide range of frequencies from 2.25 GHz, corresponding to the loop resonant frequency for a loop radius of
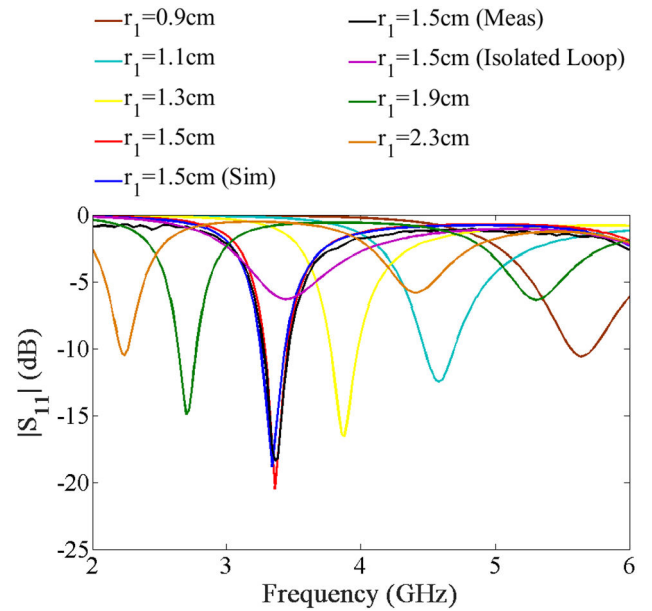

Fig. 2 *Reflection coefficient characteristics of a single-loop antenna above the cone with spherical cap with change in loop radius and comparison with an isolated loop antenna in free space: $\theta_c = 165°$, $b = 1.5$ cm, $z_1 = 2.1$ cm*
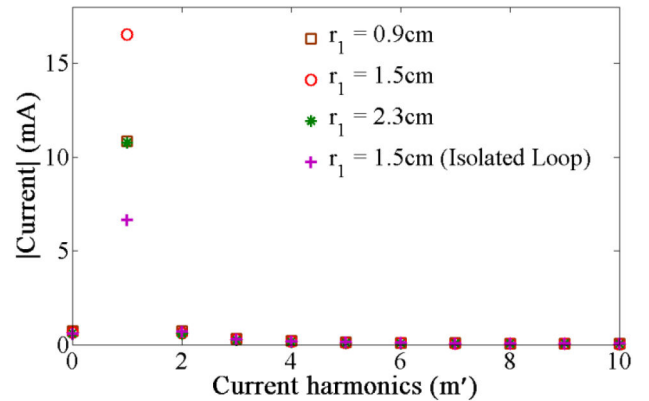

Fig. 3 *Current harmonic excitation for the loop current for the case of Fig. 2 for $r_1 = 0.9$, 1.5, 2.3 cm and an isolated loop antenna at resonance*

$r_1 = 2.3$ cm to 5.65 GHz corresponding to a loop radius of $r_1 = 0.9$ cm. The optimum reflection coefficient is obtained for a loop radius of $r_1 = 1.5$ cm at 3.37 GHz with the reflection coefficient improving steadily for $r_1 = 0.9$ cm to the optimum loop radius and degrading steadily beyond $r_1 = 1.5$ cm. It is also observed that the matching characteristics of the isolated loop antenna in free space are quite poor.

The computed results are compared with the simulated and measured results for $r_1 = 1.5$ cm. The simulations were done using the high-frequency structure simulator (HFSS) [23]. A finite conductivity of copper of 5.8×10^7 Siemens/m was used in the simulations. A length of 7λ for the cone was also considered in the simulation and measurements. For the measurement, the loop was fed through a coaxial cable through a narrow cut in the loop. An excellent agreement is observed between the computed, simulated and measured results. The magnitude of the excited current harmonics in the loop is shown in Fig. 3 for $r_1 = 0.9$, 1.5, 1.5 cm. A strong excitation of the first harmonic is observed with the strongest excitation for the optimum loop radius of $r_1 = 1.5$ cm.

The effect of the loop wire diameter on the reflection coefficient is shown in Fig. 4 for $r_1 = 1.5$ cm. Simulated results are shown in Fig. 4 since the formulation uses the thin-loop approximation. It is observed that the level of matching gradually degrades with the matching characteristics below -15 dB and the resonant frequency of the loop almost unchanged till $d_w = 3$ mm. Thereafter, a slight
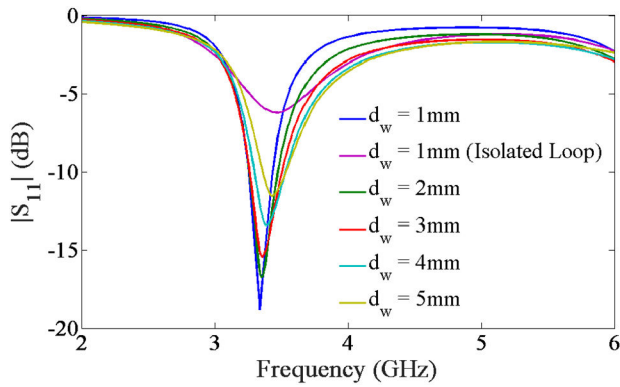
Fig. 4 *Variation in reflection coefficient characteristics of the single-loop antenna above the cone with spherical cap with change in loop wire diameter for $r_1 = 1.5$ cm and comparison with an isolated loop antenna in free space. Other parameters same as in Fig. 2*
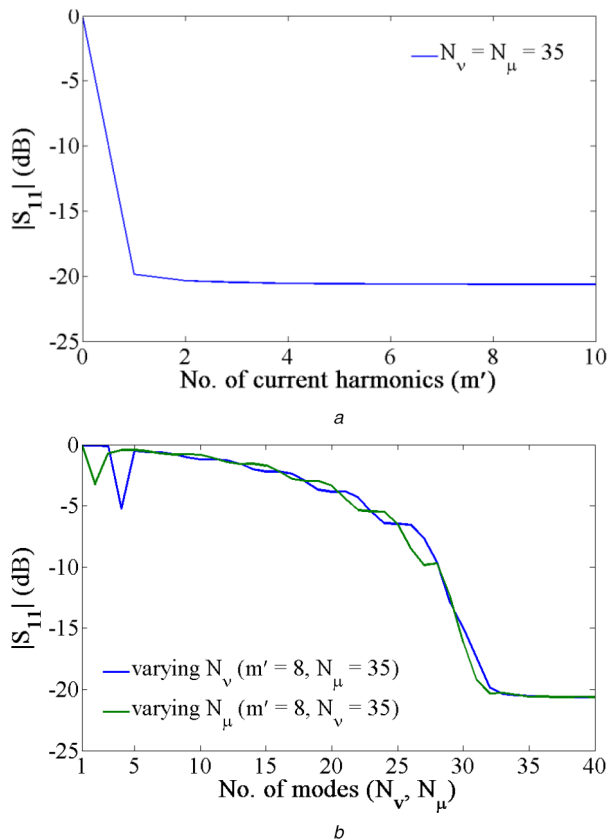

Fig. 5 *Convergence in the reflection coefficient with*
(a) Number of current harmonics, *(b)* Eigenmodes for the composite structure for the case of $r_1 = 1.5$ cm in Fig. 2

Fig. 6 *Computed, simulated and measured radiation patterns for the case of Fig. 2 for the loop antenna radius of $r_1 = 1.5$ cm at resonance*
(a) E_θ and E_ϕ patterns at $\phi = 90°$, *(b)* 3D $- E_\theta$ pattern, *(c)* 3D $- E_\phi$ pattern

right shift in the resonant frequency is observed with the reflection coefficient at 11.6 dB for $d_w = 5$ mm. The results are also compared with an isolated loop antenna in free space.

The convergence characteristics for the computation of reflection coefficient are shown in Fig. 5 with respect to the number of current harmonics and the eigenmodes of the composite structure. It is observed from Fig. 5a that 8 current harmonics are required for convergence, considering 35 eigenmodes. Fig. 5b shows the convergence characteristics with the number of eigenmodes using eight current harmonics. Convergence in the results is observed for the number of eigenmodes: $N_\nu = 35$, $N_\mu = 35$. The convergence characteristics of the current formulation depend on the loop wire radius that determines the distance between the source and the field points. The ϕ-directed loop current source is assumed to be located along the central axis of the loop according to (24), while the scattered field in (43) is computed on the loop surface when the tangential electric field
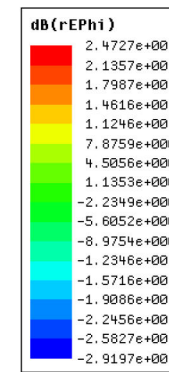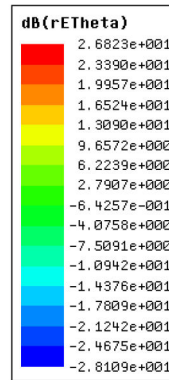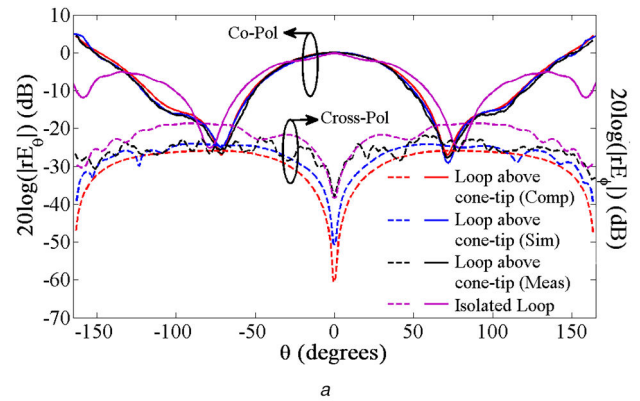
over the loop surface is enforced to be zero. As such, with smaller loop wire diameter, the source and the field points approach closer. It is observed that for the loop wire diameter $d_w = 1$ mm, convergence is achieved with eight current harmonics and the number of eigenmodes: $N_\nu = 35$, $N_\mu = 35$. On reducing the loop wire diameter to $d_w = 0.5$ mm, it is found that $N_\nu = 65$, $N_\mu = 65$ eigenmodes are needed for convergence. For a wire diameter $d_w \leq 0.4$ mm, no convergence is achieved. For the computation, the code was written in MATLAB R2018b and run on an Intel(R) Core(TM) i7-7700 CPU with 16 GB of RAM and 3.60 GHz clock speed. The average time taken by the code to compute the reflection coefficient at a single frequency point was 0.19 s. Correspondingly, the average time taken by HFSS to compute the results for the same structure was 25.70 s at a single frequency point, using a lambda refinement of 0.3 and $\Delta s = 0.02$. The peak RAM utilisation by HFSS was 4.2 GB.

The radiation characteristics of the antenna configuration for the loop radius of $r_1 = 1.5$ cm at $\phi = 90°$ at 3.37 GHz are shown in Fig. 6 and compared with the simulated results of an isolated loop. A higher directivity is obtained for the current configuration
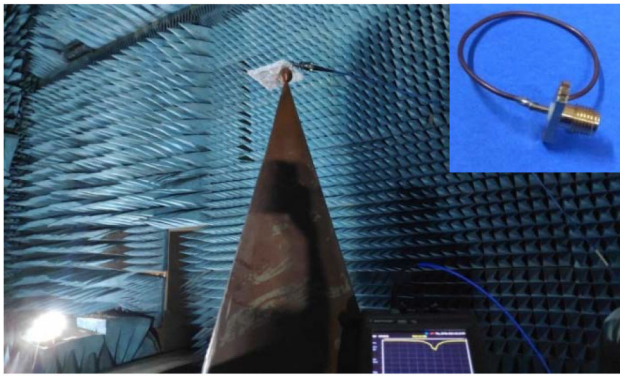
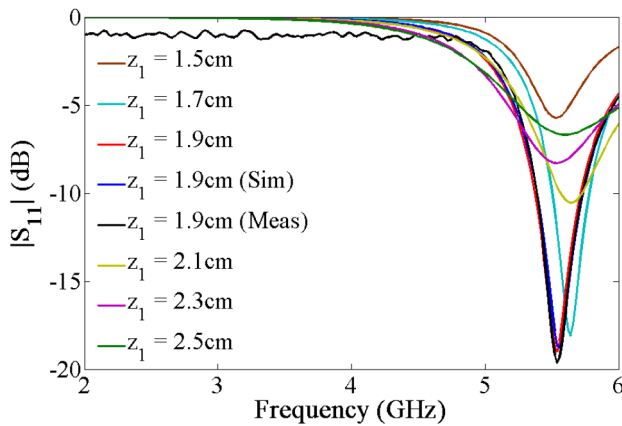**Fig. 7** *Fabricated antenna prototype with measurement setup*

Fig. 8 *Reflection coefficient characteristics of a single-loop antenna above the cone with spherical cap with change in loop height for $r_1 = 0.9$ cm in Fig. 2. Other parameters same as in Fig. 2*

Fig. 9 *Reflection coefficient characteristics of a single-loop antenna above the cone with spherical cap with change in loop height for $r_1 = 2.3$ cm in Fig. 2. Other parameters same as in Fig. 2*

Fig. 10 *Reflection coefficient characteristics of a single-loop antenna above the cone with spherical cap with change in loop height for $r_1 = 0.5$ cm. Other parameters same as in Fig. 2*

compared with the isolated loop, with the 3 dB pattern beamwidths for the current configuration and the isolated loop being 62° and 76°, respectively. The pattern is also typical of the first harmonic excitation in the loop current with E_θ as the radiation co-pol. It can also be observed that the cross-polar component E_ϕ is not affected by the presence of the cone with cap. The measured gain for the antenna configuration was at 7.69 dBi. The measured efficiency of the antenna was 97.40% that compare well with the simulated efficiency of 98.83%. The efficiency characteristics for the subsequent cases discussed are essentially similar to the above values and as such not repeated for brevity.

A photograph of the fabricated antenna prototype and the measurement setup is shown in Fig. 7. For the measurement, the loop was placed over foam to minimise scattering effects.

Next, in order to address the relatively poor matching characteristics at higher frequencies for the loop radius of $r_1 = 0.9$ cm, the position of the loop is varied to improve the impedance match. The matching characteristics in Fig. 8 show that for the optimum loop height of $z_1 = 1.9$ or 1.7 cm above the spherical cap, the reflection coefficient can be improved to below −18 dB. The computed, simulated and measured results are compared for the case $z_1 = 1.9$ cm. An excellent agreement is observed. The fundamental loop harmonic is strongly excited, as previously, with the pattern characteristics essentially similar to the previous case, and, as such, not repeated for brevity. The measured gain in this case is at 7.81 dBi at the resonant frequency of 5.54 GHz.

Next, it is investigated that if the reflection coefficient characteristics for lower frequencies could be improved. The loop radius of $r_1 = 2.3$ cm is considered corresponding to the poorest reflection coefficient characteristics. The reflection coefficient characteristics for the above case are shown in Fig. 9. It can be observed that an optimum match is obtained for the loop antenna height of $z_1 = 1.0$ cm, with an improvement in match from
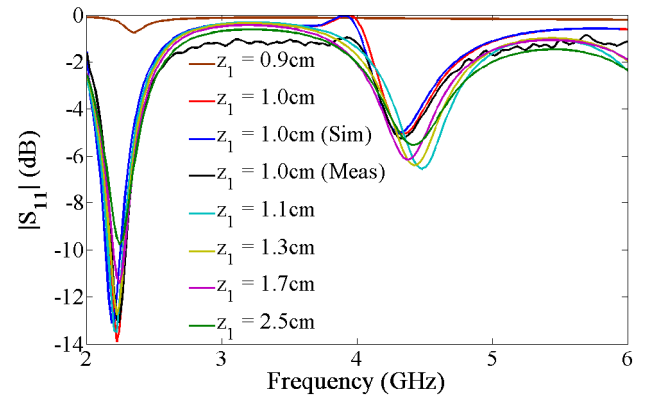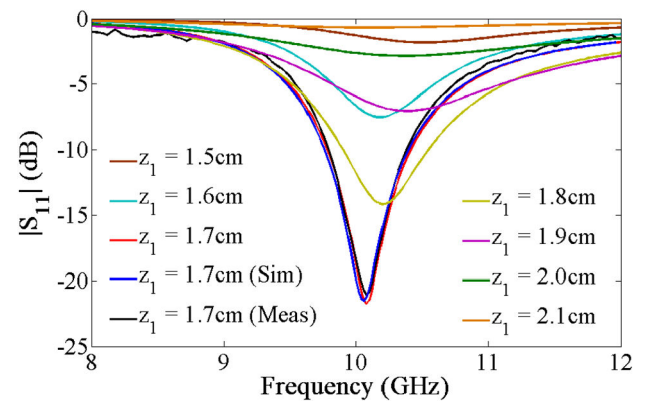
$z_1 = 2.5$ to 1.0 cm. The gain is measured at 5.40 dBi for $z_1 = 1.0$ cm at 2.22 GHz.

To extend the range of matching characteristics for the loop and the validity of the proposed method, values of loop radius outside the range shown in Fig. 2 are next chosen. Fig. 10 shows the impedance matching characteristics for a loop radius of $r_1 = 0.5$ cm that is beyond the higher-frequency range in Fig. 2. An improvement in the matching characteristics is steadily observed with an increase in loop height, with an optimum match obtained for a loop height of $z_1 = 1.7$ cm, beyond which the matching characteristics degrade. A very good agreement is observed between the computed, simulated and measured results for the optimum loop location of $z_1 = 1.7$ cm. The measured gain at the resonance frequency of 10.06 GHz is at 8.12 dBi. It is thus seen that the matching range could be very significantly extended for the loop above the cone using the spherical cap on the higher-frequency side, by varying the loop height above the cap.

To demonstrate the technique for larger loop sizes than considered in Fig. 2, a loop radius of $r_1 = 3.3$ cm is considered, corresponding to about 43% increase over the loop radius of $r_1 = 2.3$ cm in Fig. 2. The reflection coefficient characteristics are shown in Fig. 11. The best matching characteristics are observed at a loop location of $z_1 = 1.5$ cm corresponding to a resonant dip of about − 10 dB at 1.3 GHz, corresponding to the excitation of the first current harmonic. However, the matching characteristics could not be improved further with the vertical placement of the loop. To facilitate the matching, the radius of the spherical cap is varied for the optimum loop location of $z_1 = 1.5$ cm. Fig. 12 shows that the matching is significantly enhanced to about 22.64 dB at a cap radius $b = 2.3$ cm corresponding to the first current harmonic. In addition, for a cap radius of $b = 2.7$ cm, the matching characteristics at both 1.24 and 3.01 GHz are improved corresponding to the excitation of the first and second current harmonics. The mode excitation for the loop antenna at the first
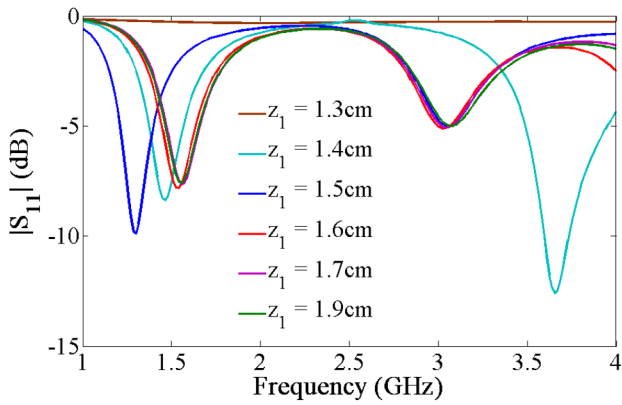
Fig. 11 *Reflection coefficient characteristics of a single-loop antenna above the cone with spherical cap with change in loop height for $r_1 = 3.3$ cm. Other parameters same as in Fig. 2*
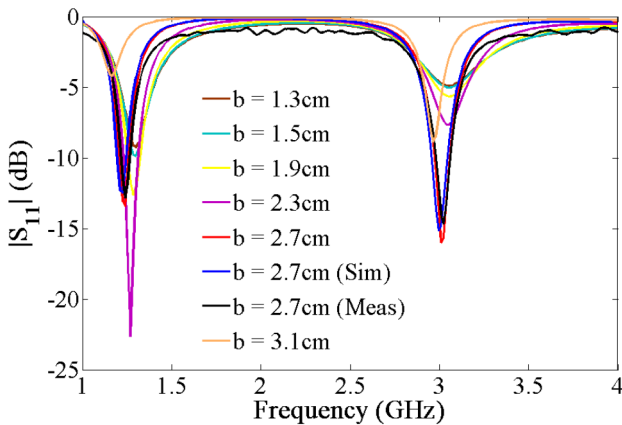

Fig. 12 *Reflection coefficient characteristics of a single-loop antenna above the cone with spherical cap with change in cap radius for $r_1 = 3.3$ cm, $z_1 = 1.5$ cm, $\theta_c = 165°$*
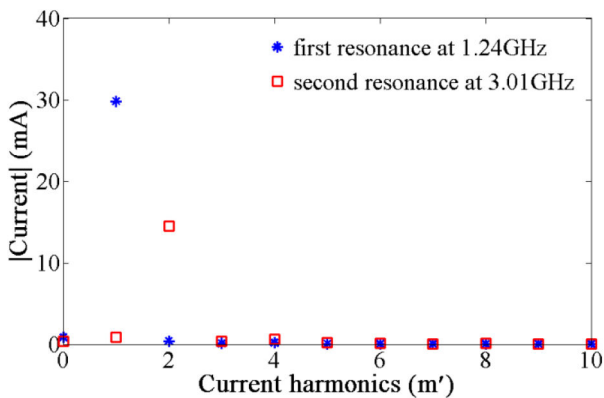

Fig. 13 *Current harmonic excitation for the loop current for $r_1 = 3.3$ cm, $z_1 = 1.5$ cm, $b = 2.7$ cm at first and second resonances in Fig. 12*

and second current harmonics for the dual-band operation for $b = 2.7$ cm is shown in Fig. 13.

The radiation characteristics corresponding to a spherical cap radius of $b = 2.7$ cm at 1.24 and 3.01 GHz are shown in Fig. 14. The pattern at the lower resonant band corresponding to the first harmonic loop current is similar to Fig. 6. The pattern characteristics at the higher resonant band are characteristic of the second harmonic with E_ϕ and E_θ as the co- and cross-polar components, respectively, at $\phi = 90°$. In addition, a monopole-like pattern with a null at $\theta = 0°$ is observed that is due to the contributions of both TE to r and TM to r terms vanishing at boresight for the second harmonic. The measured gains at 1.24 and 3.01 GHz are at 2.46 and 6.98 dBi, respectively.
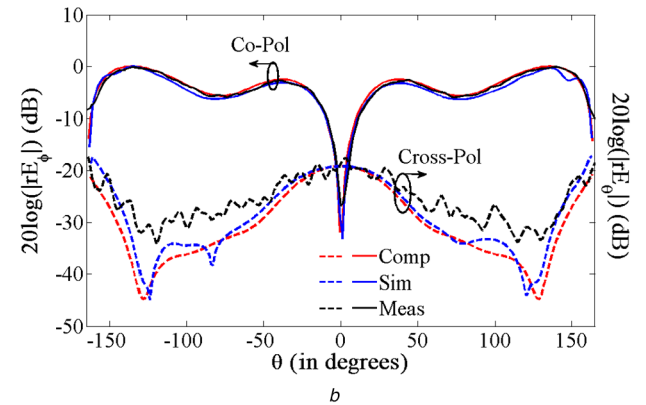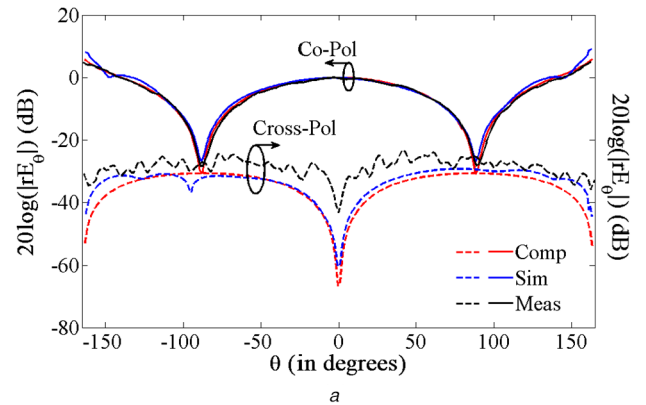

Fig. 14 *Computed, simulated and measured radiation patterns at $\phi = 90°$ in Fig. 12 for $b = 2.7$ cm at the first and second resonances*
(a) Pattern at first resonance at 1.24 GHz, *(b)* Pattern at second resonance at 3.01 GHz

The effect of a neighbouring parasitic loop on the performance of an excited loop antenna in the vicinity of the conducting cone with cap is next characterised. The situation can be practically useful in an attempt to obtain minimum interference for the excited loop when the parasitic loop is placed in proximity due to a change in operating frequency/dimensions of the excited loop. Fig. 15a shows the effect of coupling with a neighbouring loop on the matching characteristics of the primary loop, for a primary loop of radius $r_1 = 1.5$ cm. Other parameters are the same as in Fig. 2. The parasitic loop is located at the same height $z_2 = 2.1$ cm as the excited loop as its radius is varied. It is observed that matching characteristics better than -10 dB for the primary loop are obtained for the parasitic loop radius of $r_2 \leq 1.3$ and ≥ 1.6 cm.

The variation in the reflection coefficient characteristics of the primary loop with the variation in the height of the parasitic loop is shown in Fig. 15b, for similar dimensions $r_1 = r_2 = 1.5$ cm of the excited and parasitic loops. The excited loop is placed at $z_1 = 2.1$ cm as in Fig. 2. The mutual coupling due to the parasitic loop is observed to be more dominant for 1.1 cm $\leq z_2 \leq 3.6$ cm beyond which the matching characteristics of the primary loop improves over -10 dB.

4 Conclusion

A full-wave analysis of a composite structure comprising of a conducting cone with a spherical cap placed in the vicinity of a loop antenna is performed taking into account all excited current harmonics and eigenmodes in the composite structure. It is observed that the effect of the cap is to enhance the coupling of the loop antenna located above the cone tip with the cone body together with the impedance match to the loop antenna, which can be used to realise a number of efficient antenna configurations. Besides, enhancing the matching characteristics of an isolated loop, the current configuration presents a greater degree of freedom and flexibility compared with the loop around a conducting cone in [17], with enhanced matching over a wide range of loop radius and location. The antenna configuration also facilitates placement of the loop antenna above the cone tip compared with [17], potentially
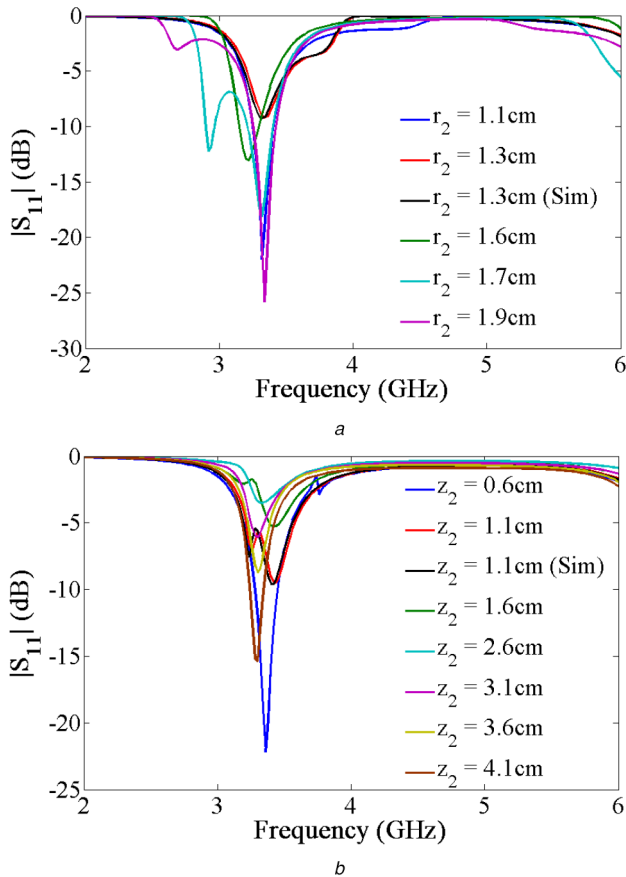
a

b

Fig. 15 *Effect of a parasitic loop on the reflection coefficient characteristics of the primary loop.* $r_1 = 1.5$ cm, $z_1 = 2.1$ cm, $b = 1.5$ cm, $\theta_c = 165°$

(a) Variation with the radius of the parasitic loop with $z_2 = z_1$, *(b)* Variation with the height of the parasitic loop with $r_2 = r_1$

enhancing signal transmission/reception and reducing interference and RF exposure on neighbouring areas together with reduced interference and scattering with the vehicle body for vehicular applications. The effect of mutual coupling of a parasitic loop on the matching characteristics of the primary excited loop is also thoroughly characterised. An excellent agreement is observed between the computed, simulated and measured results.

5 References

[1] Storer, J.E.: 'Impedance of thin-wire loop antennas', *Trans. Am. Inst. Electr. Eng.*, 1956, **75**, (pt. 1), pp. 606–619
[2] Li, L.W., Leong, M.S., Kooi, P.S.*, et al.*: 'Exact solutions of electromagnetic fields in both near and far zones radiated by thin circular-loop antennas: a general representation', *IEEE Trans. Antennas Propag.*, 1997, **45**, (12), pp. 1741–1748
[3] Harrington, R.F., Mautz, J.: 'Electromagnetic behaviour of circular wire loops with arbitrary excitation and loading', *IEE Proc.*, 1968, **115**, pp. 68–77
[4] Zhou, G., Smith, G.S.: 'An accurate theoretical model for the thin wire circular half-loop antenna', *IEEE Trans. Antennas Propag.*, 1991, **39**, (8), pp. 1167–1177
[5] Overfelt, P.L.: 'Near fields of the constant current thin circular loop antenna of arbitrary radius', *IEEE Trans. Antennas Propag.*, 1996, **44**, (2), pp. 166–171
[6] Li, L.W., Lim, C.P., Leong, M.S.: 'Method-of-moments analysis of electrically large circular-loop antennas: non-uniform currents', *IEE Proc., Microw. Antennas Propag.*, 1999, **146**, (6), pp. 416–420
[7] Li, L.W., Yeo, M.S., Leong, M.S.*, et al.*: 'Method of moments analysis of active thin circular loop antennas with closed-form currents and validity', *J. Electromagn. Waves Appl.*, 2001, **15**, (11), pp. 1551–1569
[8] An, L.N., Smith, G.S.: 'The horizontal circular loop antenna near a planar interface', *Radio Sci.*, 1982, **17**, pp. 483–502
[9] Smith, G.S., An, L.N.: 'Loop antennas for directive transmission into a material half space', *Radio Sci.*, 1983, **18**, pp. 664–674
[10] Monzon, C.: 'A loop antenna in front of a resistive sheet', *IEEE Trans. Antennas Propag.*, 1996, **44**, (3), pp. 405–412
[11] Shoamanesh, A., Shafai, L.: 'Characteristics of circular loop antennas above a lossless ground plane', *IEEE Trans. Antennas Propag.*, 1981, **29**, (3), pp. 528–529
[12] Partal, H.P., Mautz, J.R., Arvas, E.: 'Radiation from a circular loop in the presence of spherically symmetric conducting or dielectric objects', *IEEE Trans. Antennas Propag.*, 2000, **48**, (10), pp. 1646–1652
[13] Partal, H.P., Mautz, J.R., Arvas, E.: 'The exact analytical solution for large circular loops radiating around a dielectric coated conducting sphere', *IEEE Trans. Antennas Propag.*, 2009, **57**, (2), pp. 436–443
[14] Bailin, L.L., Silver, S.: 'Exterior electromagnetic boundary value problems for spheres and cones', *IRE Trans. Antennas Propag.*, 1956, **4**, (1), pp. 5–16
[15] Shavit, R.: 'Circular polarization microstrip antenna on a conical surface', *IEEE Trans. Antennas Propag.*, 1997, **45**, (7), pp. 1086–1092
[16] Lin, Y., Shafai, L.: 'Analysis of biconical microstrip antennas', *IEE Proc. H, Microw. Antennas Propag.*, 1992, **139**, (6), pp. 483–490
[17] Ghosh, B., Haque, S.M., Halder, P.: 'Analysis of arbitrary multiple-loop antennas around a conducting cone, with rotational symmetry', *IET Microw. Antennas Propag.*, 2013, **7**, (2), pp. 111–122
[18] Tai, C.T.: '*Dyadic green's functions in electromagnetic theory*' (Intext Educational Publishers, MI, USA, 1971)
[19] Harrington, R.F.: '*Time-harmonic electromagnetic fields*' (McGraw-Hill, New York, NY, USA, 1961)
[20] Ozdemir, T., Volakis, J.L.: 'Triangular prisms for edge-based vector finite element analysis of conformal antennas', *IEEE Trans. Antennas Propag.*, 1997, **45**, (5), pp. 788–797
[21] Yen, W.H., Chan, K.K.: 'Electromagnetic scattering from a thin conducting conical shell'. Proc. IEEE APS Int. Symp., Syracuse, New York, 6–10 June 1988, pp. 894–897
[22] Roan, G.T., Zaki, K.A.: 'Application of the FDTD method to the analysis of biconical antennas'. Proc. IEEE APS Int. Symp., Atlanta, Georgia, 21–26 June 1998, pp. 516–519
[23] HFSS Ver. 13. Pittsburgh: Ansoft Corporation